Chemical Science

ROYAL SOCIETY OF CHEMISTRY

EDGE ARTICLE

View Article Online
View Journal | View Issue

Cite this: *Chem. Sci.*, 2025, **16**, 2741

All publication charges for this article have been paid for by the Royal Society of Chemistry

Influence of Lewis basicity on the S^{2-} induced synthesis of 0D Cs_4PbBr_6 hexagonal nanocrystals and its implications for optoelectronics†

Yukun Liu,[a] Yangai Liu, *[a] Chenguang Yang,[a] Lefu Mei,[a] Hao Ding, [a] Ruiyu Mi[a] and Yuanyuan Zhang*[b]

Received 26th September 2024
Accepted 6th January 2025

DOI: 10.1039/d4sc06515h

rsc.li/chemical-science

Perovskite nanocrystals (NCs) with their excellent optical and semiconductor properties have emerged as primary candidates for optoelectronic applications. While extensive research has been conducted on the 3D perovskite phase, the zero-dimensional (0D) form of this promising material in the NC format remains elusive. In this paper, a new synthesis strategy is proposed. According to the Hard–Soft Acid–Base (HSAB) principle, a novel class of hexagonal semiconductor nanocrystals (Cs_4PbBr_6 HNCs) derived from 0D perovskite Cs_4PbBr_6 is synthesized by doping an appropriate amount of PbS precursor solution into bromide. These Cs_4PbBr_6 HNCs are characterized and compared in detail to $CsPbBr_3$ cubic nanocrystals ($CsPbBr_3$ CNCs) as a reference. The Cs_4PbBr_6 HNCs exhibit significantly enhanced photoluminescence (PL) compared to $CsPbBr_3$ CNCs, with an external quantum efficiency (EQE) reaching 24.19%. Furthermore, they demonstrate superior UV stability compared to $CsPbBr_3$ CNCs. Comparative analysis of their physical properties and morphology, along with detailed investigations into band structures, density of states, and lifetime decay through DFT calculations, is provided. The practical application potential is validated by encapsulating them into backlight LEDs, covering 121.5% and 90.7% of the color gamut of NTSC and Rec. Our research provides comprehensive insights into the photophysical properties of inorganic halide perovskite nanomaterials and explores their potential in the field of optoelectronics.

Introduction

In recent years, halide-based perovskite quantum dots have gained global interest for their excellent optoelectronic properties. They offer advantages such as solubility for processing, low defect density, tunability across visible to near-infrared wavelengths (400–800 nm), narrow FWHM, size-dependent effects, high quantum efficiency, and cost-effective raw materials.[1–3] As active layers in solar cells, they've boosted conversion efficiency from 3.8% in 2009 to 25.7% today, surpassing decades of silicon solar cell development.[4] In LED applications, Quantum-dot LEDs (QLEDs) exceed NTSC standards with cadmium-based ones achieving 20.5% EQE, rivalling OLEDs.[5,6] Perovskite QLEDs, with over 10% EQE, show progress, like Chiba and Kido's red-emitting QLEDs approaching 21.3% EQE.[7,8] Despite strides, commercializing them for displays and lighting remains challenging; enhanced efficiency is crucial for surpassing traditional QLEDs and OLEDs.[9]

One key factor impacting perovskite quantum dots is their structural stability, which is divided into environmental and phase stability. Environmental concerns arise from factors like ionic crystal structure, low formation energy, dynamic surface ligand bonding, high surface area, and halide vacancies, making them sensitive to polar reagents (*e.g.*, water, oxygen, light, heat, and electric fields). This sensitivity leads to crystal disintegration, changes in morphology, and phase separation.[10–12] Researchers address this by encapsulating quantum dots using physical barriers or optimizing surfaces through treatments. For example, Zhong Haizheng introduced MAPbBr-based perovskite quantum dots into PVDF, resulting in composite films with 95% quantum efficiency.[13] Joo Sung Kim achieved stable perovskite films with core/shell structures through *in situ* reactions.[14] Stasio treated $CsPbBr_3$ perovskite quantum dots with $PbBr_2$, increasing efficiency from 83% to over 95%.[15] Wang substituted oleic acid with organic phosphonic acid, maintaining $CsPbI_3$ perovskite quantum dots' performance for over 20 days.[16] Chenghao Bi replaced organic ligands with inorganic ones, enhancing quantum efficiency by mitigating charge accumulation.[17] These techniques contribute

[a]*Beijing Key Laboratory of Material Utilization of Nonmetallic Minerals and Solid Wastes, National Laboratory of Mineral Materials, School of Materials Sciences and Technology, China University of Geosciences, Beijing 100083, China. E-mail: liuyang@cugb.edu.cn*

[b]*School of Physics and Optoelectronic Engineering, Foshan University, Foshan 528000, China. E-mail: zhangyy4192@126.com*

† Electronic supplementary information (ESI) available. See DOI: https://doi.org/10.1039/d4sc06515h

to regulating perovskite surface re-crystallization, improving quantum dot quality, efficiency, and stability.

Aside from surface defects causing low quantum efficiency and instability, the dimensional morphology significantly influences perovskite quantum dot performance. Cesium lead halide perovskites, based on $[PbBr_6]^{4-}$ octahedral connectivity, exist in 3D ($CsPbBr_3$), 2D ($CsPb_2Br_5$), and 0D (Cs_4PbBr_6) structures.[18,19] 2D perovskites have $[PbX_6]^{4-}$ octahedra in layers, while 1D perovskites consist of isolated $[PbX_6]^{4-}$ octahedral chains. Complete separation of $[PbX_6]^{4-}$ octahedra is only achieved in 0D perovskites, where each octahedron is isolated. Recent interest in 0D perovskites stems from their unique photoluminescent behavior and challenging synthesis.[20] Cs_4PbBr_6 bulk crystals, reported in 1999, showed emission peaks at 545 nm, initially attributed to $CsPbBr_3$.[21] In 2016, bright green emission (PLQY = 45%) was recognized as independent, linked to rapid recombination of bound excitons (binding energy, E_b = 353 meV).[18] However, uniform-phase 0D Cs_4PbBr_6 nanocrystals remain unreported due to uncontrolled nucleation rates in traditional methods, prompting the need for a novel synthetic approach.[22,23]

In this work, we introduced lead sulfide (PbS) with a lattice constant of 5.97 Å, in the case of Cs_4PbBr_6 HNCs, their lattice constants closely resemble those of $CsPbBr_3$, with a lattice mismatch between PbS and $CsPbBr_3$ of less than 5%.[24,25] Secondly, based on the Hard–Soft Acid–Base (HSAB) principle,[26] sulfides exhibit stronger interactions with their oxide counterparts compared to Pb^{2+} and Pb^0. Lead, as a Lewis acidic atom, readily interacts with sulfide ions in multi-sulfide compounds. In comparison to bromide ions (Br^-) in $PbBr_2$, sulfide ions (S^{2-}) in PbS exhibit stronger Lewis basicity. In the precursor solution reaction, S^{2-} preferentially reacts with Pb^{2+} due to its stronger Lewis basicity, forming PbS and reducing the concentration of free Pb^{2+} ions in the solution. This partial consumption of Pb^{2+} shifts the equilibrium, making the remaining Pb^{2+} more likely to interact with Br^- to form $[PbBr_4]^{2-}$ ions. Notably, the total amount of Br^- in the system remains constant, as no additional Br^- is introduced beyond what is provided by the precursor solution. These $[PbBr_4]^{2-}$ ions subsequently combine with Cs^+ ions to form 0D Cs_4PbBr_6 crystals. Because lead sulfide (PbS) is a semiconductor material with excellent optoelectronic properties, we anticipated enhanced photovoltaic conversion efficiency by regulating absorption spectrum, optimizing band alignment, and improving charge carrier separation. Hexagonal Cs_4PbBr_6 nanocrystals (16–22 nm) were uniformly dispersed, showcasing outstanding optical and fluorescence properties, with improved long-term stability compared to traditional $CsPbBr_3$ quantum dots. This study systematically explored the impact of various PbS molar ratios on the quantum yield and luminescence of $CsPbBr_3$ quantum dots, analyzing their microscopic morphology, band structure, density of states, and overall optical properties in comparison to $CsPbBr_3$. Additionally, the research encapsulated these nanocrystals in backlighting white LEDs, evaluating their potential in optoelectronics. The findings contribute valuable insights into synthesizing zero-dimensional perovskite nanocrystals and present an effective pathway for developing highly efficient and stable perovskite quantum dots.

Experimental section

Materials

The following materials were used: $PbBr_2$ (lead bromide, Macklin, 99.9%), Cs_2CO_3 (cesium carbonate, Macklin, 99.9%), oleylamine (OAM, Macklin, 80%∼90%), oleic acid (OA, Macklin, 90%), 1-octadecene (ODE, Macklin, ≧95%), PbS (lead sulfide, Macklin, 99.9%), Methyl acetate (Macklin, 99%, with molecular sieves), *n*-hexane (Traditional Chinese medicine, 97%).

Preparation of Cs-Oleate

0.102 g cesium carbonate ($CsCO_3$) was weighed by an electronic balance, then cesium carbonate was added into a 50 mL three-necked flask together with 5 mL 1-octadecene (ODE) and 0.5 mL oleic acid (OA), and nitrogen was introduced. The mixed solution was stirred in nitrogen environment (600 rpm), and the temperature was raised to 120 °C at a rate of 5 °C min^{-1}. Then vacuum was pumped and nitrogen was introduced for three times, and then the temperature was kept for 1 hour. During the heat preservation, the change of cesium carbonate solution was observed. When the cesium carbonate was completely dissolved and the solution was clear and transparent, the temperature was continuously raised to 150 °C at a rate of 5 °C min^{-1}.

Preparation of lead halide precursor

0.188 mmol $PbBr_2$ (in the synthesis of hexagonal nanocrystals, different moles of PbS are used to replace part of lead bromide), ligand solution (0.5 mL oleic acid (OA), 0.5 mL oil amine (OAm)) and 5 mL 1-octadecene (ODE) solvent are added into a three-necked flask with electronic balance, nitrogen is introduced, the mixed solution is stirred in nitrogen atmosphere (600 rpm), and the temperature is raised to 120 °C at a rate of 5 °C min^{-1}, then vacuumized and nitrogen is introduced for three times, and then kept for 1 hour. The change of lead halide solution was observed during heat preservation. When lead halide was completely dissolved in the solution, the temperature was continuously raised to the reaction temperature at a speed of 5 °C min^{-1}, and the heat preservation was kept for 10 minutes for later use.

Preparation and purification of $CsPbBr_3$ CNCs and halide perovskite hexagonal nanocrystals Cs_4PbBr_6 HNC

Cesium oleate precursor was heated to 120 °C, and then 1 mL was quickly injected into lead precursor by syringe, and the solution instantly changed from clear and transparent to muddy oil. The reaction must stop immediately within 5 seconds. Therefore, a cold water bath should be set nearby (Reference Fig. 1). Purification scheme: the synthesized crude solution is collected in a 50 mL cone centrifuge. Methyl acetate was added to the crude solution in a volume ratio of 1 : 1 and the mixture was centrifuged at 7800 rpm (∼7140 *cf.*) for 10 minutes. The supernatant containing excess ligands and unreacted by-products was discarded and the precipitate was dispersed in

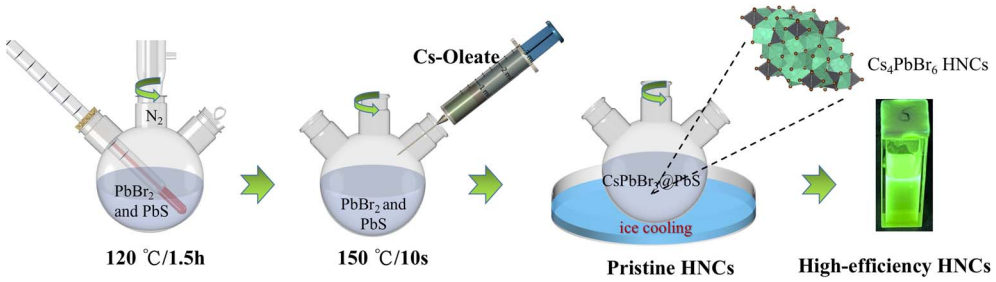

Fig. 1 Synthesis of $CsPbBr_3$ perovskite NCs.

a mixture of 5 mL *n*-hexane and 5 mL methyl acetate. The mixture was again centrifuged at 7500 rpm (~6600 rcf) for 10 minutes. The precipitate was dissolved in 2 mL *n*-hexane.

Characteristic test

The phase structures were analyzed using a D8 ADVANCE X-ray diffractometer (Bruker, Germany) with a CuK X-ray source, a scanning step size of 0.05°, and a 2θ range of 15°–60°. X-ray Photoelectron Spectroscopy (XPS) was conducted using the Thermo 250Xi instrument. The transmission electron microscope used for experimental testing is the JEOL JEM-2100F model. The emission spectra and variable temperature spectrum were examined using a Hitachi F-4700 fluorescence spectrophotometer (150 W xenon lamp). EQE was measured by Quantaurus-QY Plus C13534-12, Hamamatsu Photonics. The PL decay curves were measured by a fluorescence spectrophotometer (Edinburgh FSL1000) using a 60 W μs flash lamp as an excitation light source. A UV-visible-near-infrared spectrophotometer was used to get the diffuse reflectance spectrum (UH4150). Packaged LED test instrument use: OHSP-350 M LED Fast-Scan Spectrophotometer (350–1050 nm).

LED packaging parameters

Sanan Optoelectronics Company's 3 W, ~445–450 nm LED chip is used in the actual LED packaging, Cs_4PbBr_6 HNCs and KSF red phosphors (Ganzhou Zhonglan Rare Earth New Material Technology) are co-encapsulated with a red-to-green phosphor mass ratio of approximately 1 : 2. UV-curable adhesive (Leaftop 6300) is used with a phosphor-to-adhesive mass ratio of 1 : 1.

Results and discussion

Fig. 2(a) shows the X-ray diffraction (XRD) patterns of Cs_4PbBr_6 HNCs and $CsPbBr_3$ CNCs, and we provide standard cards for $CsPbBr_3$ (PDF#75-0412), Cs_4PbBr_6 (PDF#54-0750), and PbS (PDF#78-1900) for comparison. $CsPbBr_3$ CNCs correspond to the cubic phase of $CsPbBr_3$ quantum dots, belonging to the $pm\bar{3}m$ space group, and the sharp diffraction peaks indicate good crystallinity of the samples. In comparison, Cs_4PbBr_6 HNCs, when compared with the standard card Cs_4PbBr_6 (PDF#54-0750), fully confirm that our samples mainly possess a 0D perovskite structure, though they are also embedded with some $CsPbBr_3$ nanocrystals, consistent with previous reports. The luminescence mechanism of Cs_4PbBr_6 is more likely associated with trace amounts of embedded $CsPbBr_3$.[27–29] To further analyze the surface composition and structure of Cs_4PbBr_6 HNCs, we conducted X-ray photoelectron spectroscopy (XPS) on Cs_4PbBr_6 HNCs and $CsPbBr_3$ CNCs. Fig. 2(b) represents the full spectra of Cs_4PbBr_6 HNCs and $CsPbBr_3$ CNCs, showing absorption peaks for the three basic elements Cs, Pb, and Br. There are no significant differences in the Cs 3d, Pb 4f, and Br 3d absorption peaks. However, since we doped PbS into the precursor solution during the preparation process, let's focus on the Pb 4f absorption peaks, as shown in Fig. 2(c). Both samples exhibit Pb 4f peaks at approximately ~142.8 eV and ~137.9 eV, ~142.6 eV and ~137.7 eV, respectively. The peak shapes are smooth and similar, with slight shifts possibly attributed to sample non-uniformity. Transmission electron microscopy (TEM) was employed to analyze the morphology and size variations of the two types of quantum dots. Fig. 2(d) displays the morphology of $CsPbBr_3$ CNCs, revealing uniformly sized cubes with dimensions around 10 nm. It's worth noting that some quantum dots in the image have small "dark spots," which are more pronounced in Fig. 2(d). These small "dark spots" are metallic lead and are typically closely associated with the exposed lead on the quantum dot surface.[30] Fig. 2(e) illustrates the morphology of Cs_4PbBr_6 HNCs, showing a uniform hexagonal shape. This is attributed to Cs_4PbBr_6 belonging to the $R\bar{3}c$ space group, with dimensions around 22 nm. The reverse transition from 3D to 0D usually accompanies size expansion, indicating the presence of a dissolution reprecipitation process.[31,32] To determine the composition and elemental distribution of the synthesized Cs_4PbBr_6 nanocrystals, TEM-EDS (Transmission Electron Microscopy-Energy Dispersive Spectroscopy) analysis was conducted, as shown in Fig. 2(f). The results revealed that the primary elements in the sample were Cs, Pb, and Br, consistent with the zero-dimensional Cs_4PbBr_6 perovskite structure. In addition, a weak sulfur (S) signal was detected, which can be attributed to the introduction of PbS in the precursor solution during the synthesis process. The mapping images showed that Cs, Pb, and Br were uniformly distributed across the nanocrystals, indicating the homogeneity of the Cs_4PbBr_6 phase. Interestingly, the sulfur distribution overlapped with that of Pb, suggesting that PbS was effectively incorporated into the nanocrystals during the reaction. This incorporation may influence the structural stability and optoelectronic properties of the material. The sulfur signal, while

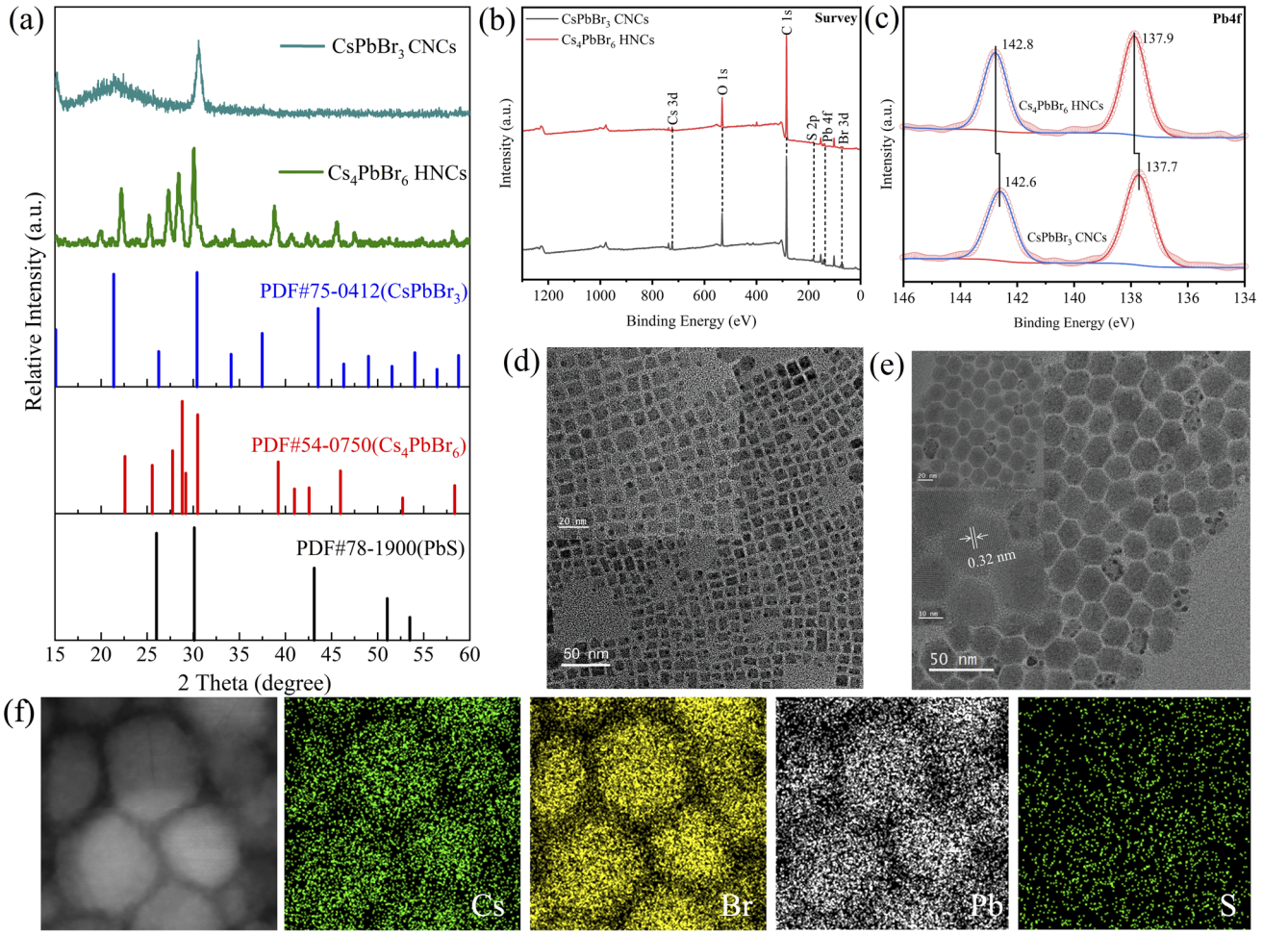

Fig. 2 (a) X-ray diffraction (XRD) patterns of Cs_4PbBr_6 HNCs and $CsPbBr_3$ CNCs. (b) The full spectra of Cs_4PbBr_6 HNCs and $CsPbBr_3$ CNCs. (c) Pb4f absorption peak spectra of Cs_4PbBr_6 HNCs and $CsPbBr_3$ CNCs. (d and e) Are TEM spectra of Cs_4PbBr_6 HNCs and $CsPbBr_3$ CNCs, respectively. (f) Analysis of TEM-EDS distribution of Cs_4PbBr_6.

relatively weak, was clearly observed, reflecting its role as a structural modifier rather than a primary component. These findings underscore the effectiveness of using PbS as a precursor to modulate the reaction pathway and optimize the growth of Cs_4PbBr_6 nanocrystals.

As depicted in Fig. 3, band structures and density of states for $CsPbBr_3$ and Cs_4PbBr_6 were computed using density functional theory (DFT).[33–35] To be specific, the three-dimensional $CsPbBr_3$ perovskite boasts a corner-sharing $[PbBr_6]^{4-}$ octahedral framework that extends across all three dimensions. In stark contrast, the zero-dimensional Cs_4PbBr_6 perovskite comprises a cluster of $[PbBr_6]^{4-}$ octahedra isolated by Cs^+ ions. Due to the isolation of $[PbBr_6]^{4-}$ octahedra, orbital coupling between the valence band (Pb 6s and Br 4p) and the conduction band (Pb 6p and Br 4p) is weaker, resulting in a band structure that is both flat and exhibits a wide band gap. From the band structures, it is evident that Cs_4PbBr_6 possesses a band gap of 4.79 eV, with the valence band maximum (VBM) situated at the Brillouin zone *T* point and the conduction band minimum (CBM) at the Brillouin zone Γ point. In contrast, $CsPbBr_3$ exhibits a band gap of 2.34 eV, with the VBM located at the Brillouin zone Γ point. This indicates that both materials exhibit characteristics of direct band gaps, which aligns with the trend of increasing band gap as the structural dimension decreases. In both scenarios, the conduction band minimum (CBM) is primarily composed of Pb 6p and Br 4p states, while the valence band maximum (VBM) consists of Pb 6s and Br 4p states. Nevertheless, in the case of the zero-dimensional perovskite, these Pb 6s, 6p, and Br 4p atomic orbitals remain decoupled because the $[PbBr_6]^{4-}$ octahedra are isolated within the electronic zero-dimensional structure. This fundamental isolation contributes significantly to the large band gap observed in zero-dimensional perovskites. Despite their substantial band gaps, zero-dimensional perovskites serve not only as suitable dielectric matrices but also play a pivotal role in enhancing the photoluminescent quantum yield of green-emitting centers by efficiently transferring the energy emitted by Pb^{2+} ions to green emission centers.[21,36,37]

Examining the photophysical features of unique Cs4$PbBr_6$ hexagonal nanocrystals (HNCs) in comparison to standard $CsPbBr_3$ cubic nanocrystals (CNCs, used as a reference), we assessed their photoluminescence (PL) and absorption spectra.

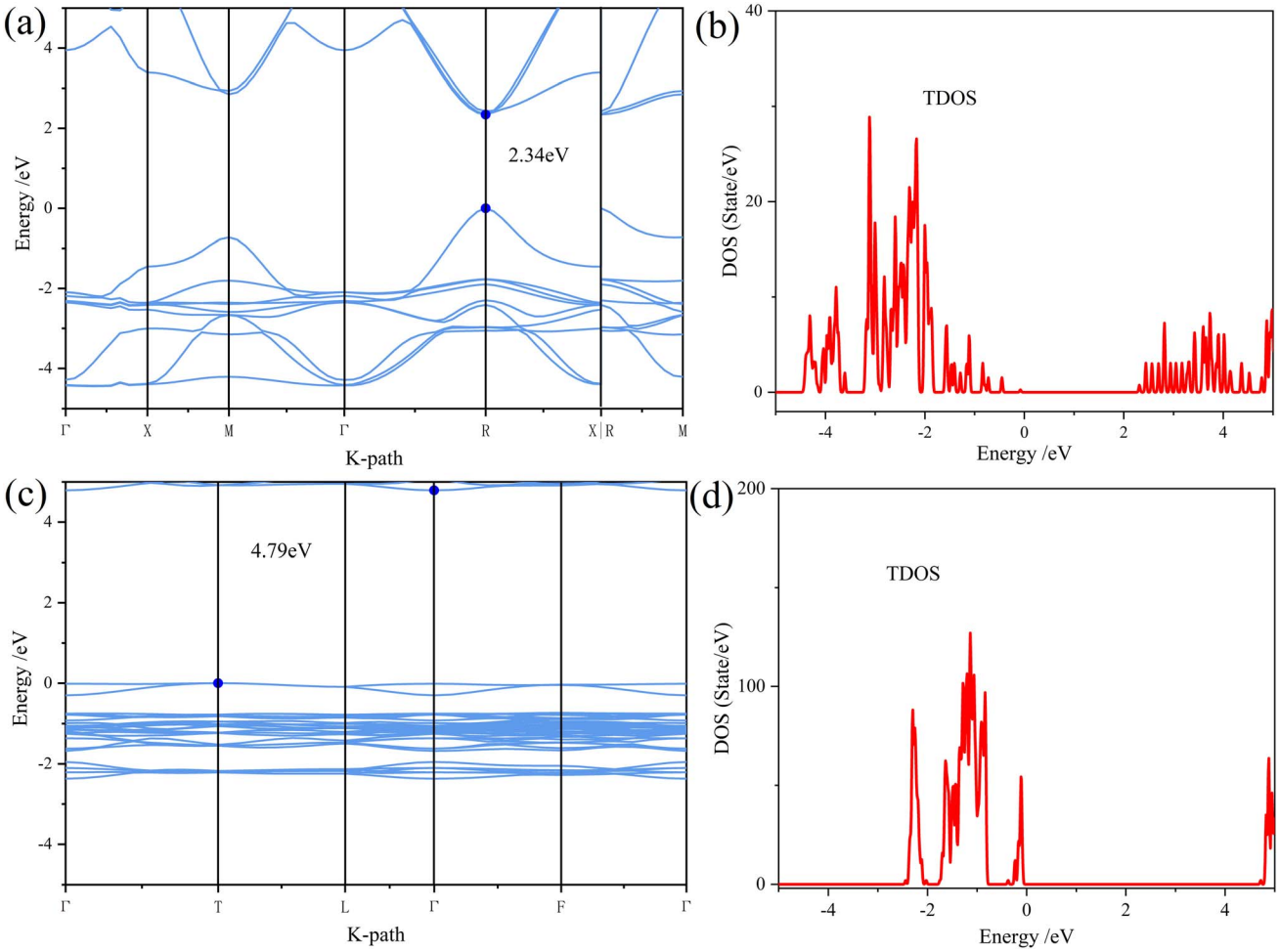

Fig. 3 The electronic band structures (a) and TDOS (b) of $CsPbBr_3$; the electronic band structures (c) and TDOS (d) of Cs_4PbBr_6 by density functional theory (DFT) calculations.

Fig. 4(a) illustrates under 365 nm excitation, the spectra displayed narrow-band emission peaking between 500 nm and 550 nm, resembling the typical green emission of $CsPbBr_3$ quantum dots. The emission peak consistently blueshifted with increasing PbS doping concentration, reaching its maximum shift at a 7% mmol molar ratio in the precursor solution. Regarding the mechanism behind the blueshift observed after doping PbS, this phenomenon is primarily attributed to the quantum confinement effect. As PbS nanoparticles are incorporated into the Cs_4PbBr_6 matrix, the spatial confinement of charge carriers increases, leading to a widening of the bandgap. This results in the observed blueshift in the emission peak.[38] Subsequent spectra with PbS doping exceeding 8% mmol were notably suppressed, losing the characteristic emission peak. This implies that suitable PbS doping ratios in the $PbBr_2$ precursor solution are critical for forming Cs_4PbBr_6 HNCs. The emission spectra of Cs_4PbBr_6 HNCs exhibited significantly enhanced intensity, yielding an EQE of 24.19%, possibly due to stronger multiphoton effects, enabling more photon absorption and intense luminescence. This suggests that the material can absorb more photons upon excitation, leading to more intense luminescence. This difference can be attributed to the rapid electron–hole bimolecular recombination behavior of Cs_4PbBr_6 HNCs, which is related to photoluminescence.[39,40] Furthermore, Cs_4PbBr_6 possesses a larger lattice structure, which renders it more stable under variations in temperature and humidity. The softness of 0D perovskite was evidenced by the Young's modulus measurement, where $CsPbBr_3$ (21.5 GPa) was found to be twice as hard as Cs_4PbBr_6 (12.1 GPa).[41] Maintaining luminescent performance, the lead-deficient nature of Cs_4PbBr_6 introduces Pb ions as dopants, forming tightly bound Frenkel excitons that enhance radiative recombination, resulting in high emissions across various material forms. Spectra of Cs_4PbBr_6 HNCs exhibit broadening, likely due to size distribution non-uniformity, impacting particle or crystal size. Additionally, lead sulfide (PbS) doping introduces electronic energy levels interacting with perovskite bands, broadening sensitivity to wavelengths. Fig. 4(b) details absorption spectra, revealing $CsPbBr_3$ perovskite quantum dots' exciton absorption near 514 nm. In contrast, Cs_4PbBr_6 HNCs show two peaks (293 nm and 523 nm), indicating a wider bandgap requiring higher energy for electron excitation. Cs_4PbBr_6 HNCs absorb shorter-wavelength light than two-dimensional perovskite quantum dots. The distinct absorption spectra confirm exciton

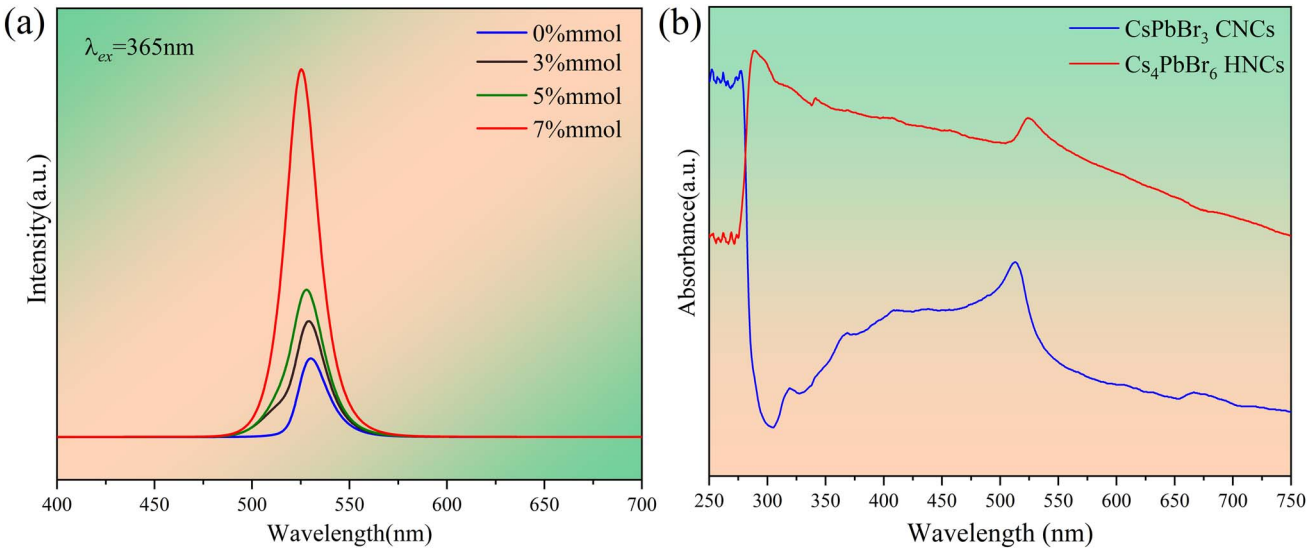

Fig. 4 (a) Emission spectra of $CsPbBr_3$ CNCs and Cs_4PbBr_6 HCNs doped with PbS with different molar ratios. (b) Absorption spectra of $CsPbBr_3$ CNCs and Cs_4PbBr_6 HCNs.

recombination dominance in $CsPbBr_3$, while less prominent exciton absorption in Cs_4PbBr_6 HNCs raises suspicion of embedded $CsPbBr_3$ nanocrystals, supporting XRD analysis.

To gain further insights into their optical performance, we conducted fluorescence lifetime tests on both $CsPbBr_3$ CNCs and Cs_4PbBr_6 HNCs, as shown in Fig. 5(a) and (b). We employed a quadratic fitting to correspond to two bright centers:

$$I(t) = I_0 + A_1 \exp(-t/\tau_1) + A_2 \exp(-t/\tau_2) \quad (1)$$

where A_1 and A_2 are constants, I_0 and $I_{(t)}$ represent the initial and instantaneous emission intensities, respectively. The fast and slow lifespan are τ_1 and τ_2, respectively. The average life can be determined using the following formula:

$$\tau^* = (A_1\tau_1^2 + A_2\tau_2^2)/(A_1\tau_1 + A_2\tau_2) \quad (2)$$

The average lifetimes in Fig. 5(a) and 4(b) were calculated using the aforementioned procedure. Through our calculations, we observed a significant reduction in fluorescence lifetime for Cs_4PbBr_6 HNCs compared to $CsPbBr_3$ CNCs, with τ_{amp} decreasing from 18.14 ns to 8.92 ns and τ_{int} decreasing from 55.76 ns to 15.32 ns. The reduction in quantum dot fluorescence lifetime may be attributed to fluorescence resonance energy transfer (FRET): to understand the photophysical properties of Cs_4PbBr_6 HNCs in comparison to $CsPbBr_3$, we performed Density Functional Theory (DFT) calculations. Cs_4PbBr_6 HNCs exhibited a wider bandgap structure compared to $CsPbBr_3$, indicating a larger bandgap in Cs_4PbBr_6 HNCs. In Cs_4PbBr_6 HNCs, due to the higher binding energy, electrons and holes were more prone to recombine. This led to an increased rate of electron–hole recombination, resulting in a shorter fluorescence lifetime. Another contributing factor is that the lattice structure of Cs_4PbBr_6 HNCs is relatively complex, with a higher number of atoms. This complexity may enhance lattice vibrations and electron–phonon interactions, prompting electrons and holes to recombine more rapidly. The effective mass of electrons and holes in the material also affects the recombination rate. Smaller effective masses typically result in faster electron and hole recombination, which may be another reason for the shorter fluorescence lifetime observed in Cs_4PbBr_6 HNCs. To assess the potential applications of Cs_4PbBr_6 HNCs, we investigated their stability under UV conditions, as shown in Fig. 5(c). With increasing UV irradiation time, the luminescence intensity of Cs_4PbBr_6 HNCs initially increased before decreasing. The initial enhancement was likely due to the excitation of charge carriers within the Cs_4PbBr_6 HNCs quantum dots by the onset of UV irradiation, leading to an increase in fluorescence intensity. This is because UV light has sufficiently high energy to excite electrons from the valence band to the conduction band, generating excited states and enhancing fluorescence emission. As UV irradiation continued, complex surface reactions and charge carrier capture processes might occur. These processes could lead to the recombination or capture of excitons (electron–hole pairs), reducing the number of excitons available for emission. Additionally, prolonged UV irradiation may cause changes in the material properties of Cs_4PbBr_6 HNCs, such as lattice distortions or the formation of surface defects. These changes could result in decreased fluorescence efficiency, leading to a reduction in luminescence intensity. However, when considering the overall picture, the luminescence intensity of Cs_4PbBr_6 HNCs still maintained approximately 84.43% after 120 minutes of continuous UV irradiation, demonstrating excellent UV stability. We attribute this stability to the larger crystal structure of Cs_4PbBr_6, where lead ions are surrounded by four calcium ions. This crystal structure is more stable compared to the smaller crystal structure of $CsPbBr_3$. This greater stability enables Cs_4PbBr_6 to better resist structural changes induced by

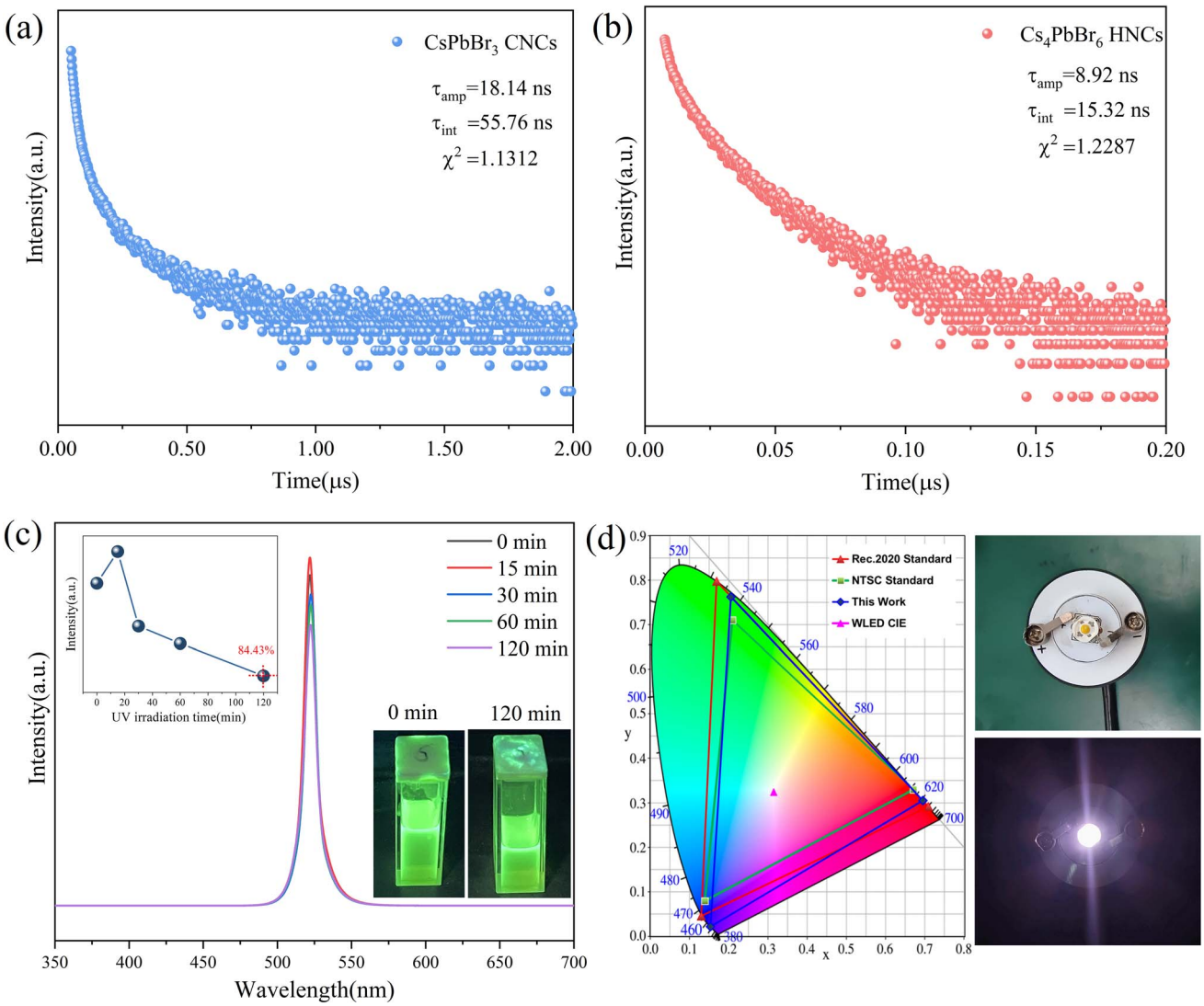

Fig. 5 (a) $CsPbBr_3$ CNCs fluorescence lifetime decay curve. (b) Cs_4PbBr_6 HNCs fluorescence lifetime decay curve. (c) UV spectral stability of Cs_4PbBr_6 HNCs under different time UV irradiation. (d) Cs_4PbBr_6 HNCs backlight white LED package diagram and CIE diagram.

UV light. The slower migration speed of lead ions in Cs_4PbBr_6 further reduces instability caused by ion migration under illumination. In contrast, $CsPbBr_3$, with its faster lead ion migration, is more prone to performance degradation, further underscoring its potential for use in optoelectronic devices.

The application value of Cs_4PbBr_6 HNCs was finally validated by encapsulating them as a backlight white LED. As shown in Fig. 5(d), the Cs_4PbBr_6 HNCs backlight white LED package diagram and CIE diagram demonstrate excellent performance. Various data are presented in tabular form below. Typically, color gamut values are used to evaluate the color performance of LED displays or lighting devices. Color gamut values are commonly used to describe the color reproduction capability and color range displayed by LEDs. As shown in Table 1, Cs_4PbBr_6 HNCs encapsulated as a backlight white LED exhibit a 1931 Gamut (NTSC %) of 121.5% and a 1931 Gamut (Rec. 2020%) of 90.7%, demonstrating outstanding performance and application value. The test parameters for the encapsulated LED are shown in Table 2. Currently, backlight white LEDs generally use rare-earth materials such as Gallium Phosphide (GaP) or Gallium Nitride (GaN) as the luminescent materials. These materials are used in LED chips to generate white light through different luminescent layers and structures. Quantum dots, as the backlight source for LEDs, can achieve a wider color gamut, providing richer and more realistic colors. This is crucial for

Table 1 Color gamut results obtained by calculating three-color coordinates separated by RGB

Product	White	Red	Green	Blue
x	0.315	0.694	0.206	0.154
y	0.324	0.305	0.762	0.022
u'	0.201	0.526	0.070	0.209
v'	0.466	0.521	0.585	0.067
1931 Gamut (NTSC %) =	121.5%			
1931 Gamut (Rec. 2020%) =	90.7%			

Table 2 Package LED luminosity parameters

Serial number	Luminous efficiency (lm W^{-1})	Φ (lm)	Gamut index Rg	Color purity (%)	Light and dark vision ratio S/P	Chromaticity coordinates (x, y)
20 mA	2.63	0.23	124.51	6.9	2.084	0.315, 0.324
40 mA	2.67	0.46	126.01	7.0	2.079	0.316, 0.320
60 mA	3.92	0.63	132.50	11.1	2.157	0.317, 0.296
80 mA	3.19	0.69	141.05	34.5	2.355	0.312, 0.240
100 mA	2.74	0.75	149.29	47.2	2.586	0.307, 0.203
120 mA	2.49	0.83	154.00	52.1	2.682	0.306, 0.189

High Dynamic Range (HDR) displays and achieving higher-quality visual effects. Furthermore, they offer precise color control: quantum dot colors can be precisely controlled by adjusting the size of the quantum dots, enabling very accurate color matching. Quantum dots can also increase brightness and efficiency in LEDs since they can convert unwanted wavelengths into visible light, reducing energy waste.

Conclusions

In conclusion, a novel strategy based on the introduction of lead sulfide (PbS) with a crystal structure and lattice constant similar to $CsPbBr_3$ perovskite quantum dots precursor solution has successfully synthesized Cs_4PbBr_6 hexagonal nanocrystals (HNCs). To comprehensively study their photophysical properties, this study utilized $CsPbBr_3$ cubic nanocrystals (CNCs) as a reference material and investigated their phase, surface elements, and microstructure. Interestingly, the addition of an appropriate amount of PbS to the precursor solution transformed Cs_4PbBr_6 HNCs from uniform cubes of approximately 10 nm in size to uniform hexagons of around 22 nm. By performing DFT calculations of their band structures and density of states, the differences and reasons were analyzed in detail. Comparative analyses of their optical properties, including photoluminescence (PL), absorption spectra, and lifetime decay, were conducted, demonstrating the superior performance of Cs_4PbBr_6 HNCs. Furthermore, the UV stability of Cs_4PbBr_6 HNCs was tested, and their performance when encapsulated into backlight white LEDs was evaluated. Our research results provide comprehensive insights into the rich optical characteristics of inorganic halide perovskite Cs_4PbBr_6 HNCs, indicating the greater potential of this type of perovskite nanomaterial in applications spanning display technology, LED lighting, nonlinear optical imaging, and traditional electronic switching devices.

Data availability

All experimental data, procedures for data analysis, and pertinent data sets are provided in the ESI.†

Author contributions

Under the supervision of Yangai Liu, Yukun Liu carried out all experiments and analyses related to XRD, TEM, PL, DFT, LED packaging, *etc.* Yukun Liu composed the original draft with the contributions of Lefu Mei, Hao Ding, and Ruiyu Mi. Chenguang Yang and Yuanyuan Zhang assisted in some experimental operations and the refinement of the article's language. All authors contributed to the final version.

Conflicts of interest

There are no conflicts to declare.

Acknowledgements

This work was supported by the National Natural Science Foundation of China (Grant No. 52072348, No.U22A2030 and Grant No. 52104272),and the Fundamental Research Funds for the Central Universities (Grant No. 2652020020).

References

1 A. Swarnkar, A. R. Marshall, E. M. Sanehira, B. D. Chernomordik, D. T. Moore, J. A. Christians, T. Chakrabarti and J. M. Luther, Quantum dot-induced phase stabilization of α-$CsPbI_3$ perovskite for high-efficiency photovoltaics, *Science*, 2016, **354**, 92–95.
2 B. Saparov and D. B. Mitzi, Organic-Inorganic Perovskites: Structural Versatility for Functional Materials Design, *Chem. Rev.*, 2016, **116**, 4558–4596.
3 L. Protesescu, S. Yakunin, M. I. Bodnarchuk, F. Krieg, R. Caputo, C. H. Hendon, R. X. Yang, A. Walsh and M. V. Kovalenko, Nanocrystals of Cesium Lead Halide Perovskites ($CsPbX_3$, X = Cl, Br, and I): Novel Optoelectronic Materials Showing Bright Emission with Wide Color Gamut, *Nano Lett.*, 2015, **15**, 3692–3696.
4 C. D. Bailie and M. D. McGehee, High-efficiency tandem perovskite solar cells, *MRS Bull.*, 2015, **40**, 681–685.
5 P. Amini, M. Dolatyari, A. Rostami, G. Rostami, S. Mathur and P. Torabi, High-Performance Solution Processed Inorganic Quantum-Dot LEDs, *IEEE Trans. Nanotechnol.*, 2015, **14**, 911–917.
6 J. Kim, H. J. Shim, J. Yang, M. K. Choi, D. C. Kim, J. Kim, T. Hyeon and D. H. Kim, Ultrathin Quantum Dot Display Integrated with Wearable Electronics, *Adv. Mater.*, 2017, **29**, 6.
7 D. B. Han, M. Imran, M. J. Zhang, S. Chang, X. G. Wu, X. Zhang, J. L. Tang, M. S. Wang, S. Ali, X. G. Li, G. Yu,

J. B. Han, L. X. Wang, B. S. Zou and H. Z. Zhong, Efficient Light-Emitting Diodes Based on *in Situ* Fabricated $FAPbBr_3$ Nanocrystals: The Enhancing Role of the Ligand-Assisted Reprecipitation Process, *ACS Nano*, 2018, **12**, 8808–8816.

8 F. Yan, J. Xing, G. C. Xing, L. Quan, S. T. Tan, J. X. Zhao, R. Su, L. L. Zhang, S. Chen, Y. W. Zhao, A. Huan, E. H. Sargent, Q. H. Xiong and H. V. Demir, Highly Efficient Visible Colloidal Lead-Halide Perovskite Nanocrystal Light-Emitting Diodes, *Nano Lett.*, 2018, **18**, 3157–3164.

9 T. Chiba, Y. Hayashi, H. Ebe, K. Hoshi, J. Sato, S. Sato, Y. J. Pu, S. Ohisa and J. Kido, Anion-exchange red perovskite quantum dots with ammonium iodine salts for highly efficient light-emitting devices, *Nat. Photonics*, 2018, **12**, 681.

10 K. A. Bush, K. Frohna, R. Prasanna, R. E. Beal, T. Leijtens, S. A. Swifter and M. D. McGehee, Compositional Engineering for Efficient Wide Band Gap Perovskites with Improved Stability to Photoinduced Phase Segregation, *ACS Energy Lett.*, 2018, **3**, 428–435.

11 C. Rodà, A. L. Abdelhady, J. Shams, M. Lorenzon, V. Pinchetti, M. Gandini, F. Meinardi, L. Manna and S. Brovelli, O_2 as a molecular probe for nonradiative surface defects in $CsPbBr_3$ perovskite nanostructures and single crystals, *Nanoscale*, 2019, **11**, 7613–7623.

12 Z. Y. Dang, B. Dhanabalan, A. Castelli, R. Dhall, K. C. Bustillo, D. Marchelli, D. Spirito, U. Petralanda, J. Shamsi, L. Manna, R. Krahne and M. P. Arciniegas, Temperature-Driven Transformation of $CsPbBr_3$ Nanoplatelets into Mosaic Nanotiles in Solution through Self-Assembly, *Nano Lett.*, 2020, **20**, 1808–1818.

13 Q. C. Zhou, Z. L. Bai, W. G. Lu, Y. T. Wang, B. S. Zou and H. Z. Zhong, In Situ Fabrication of Halide Perovskite Nanocrystal-Embedded Polymer Composite Films with Enhanced Photoluminescence for Display Backlights, *Adv. Mater.*, 2016, **28**, 9163.

14 J. S. Kim, J. M. Heo, G. S. Park, S. J. Woo, C. Cho, H. J. Yun, D. H. Kim, J. Park, S. C. Lee, S. H. Park, E. Yoon, N. C. Greenham and T. W. Lee, Ultra-bright, efficient and stable perovskite light-emitting diodes, *Nature*, 2022, **611**, 688.

15 F. Di Stasio, S. Christodoulou, N. J. Huo and G. Konstantatos, Near-Unity Photoluminescence Quantum Yield in $CsPbBr_3$ Nanocrystal Solid-State Films via Postsynthesis Treatment with Lead Bromide, *Chem. Mat.*, 2017, **29**, 7663–7667.

16 C. J. Wang, A. S. R. Chesman and J. J. Jasieniak, Stabilizing the cubic perovskite phase of $CsPbI_3$ nanocrystals by using an alkyl phosphinic acid, *Chem. Commun.*, 2017, **53**, 232–235.

17 C. H. Bi, Z. W. Yao, J. C. Hu, X. Y. Wang, M. Q. Zhang, S. Y. Tian, A. Q. Liu, Y. Lu, N. H. de Leeuw, M. L. Sui and J. J. Tian, Suppressing Auger Recombination of Perovskite Quantum Dots for Efficient Pure- Blue-Light-Emitting Diodes, *ACS Energy Lett.*, 2022, **8**, 731–739.

18 M. I. Saidaminov, J. Almutlaq, S. Sarmah, I. Dursun, A. A. Zhumekenov, R. Begum, J. Pan, N. Cho, O. F. Mohammed and O. M. Bakr, Pure Cs_4PbBr_6: Highly Luminescent Zero Dimensional Perovskite Solids, *ACS Energy Lett.*, 2016, **1**, 840–845.

19 T. C. Sum and N. Mathews, Advancements in perovskite solar cells: photophysics behind the photovoltaics, *Energy Environ. Sci.*, 2014, **7**, 2518–2534.

20 O. F. Mohammed, Outstanding Challenges of Zero-Dimensional Perovskite Materials, *J. Phys. Chem. Lett.*, 2019, **10**, 5886–5888.

21 M. Nikl, E. Mihokova, K. Nitsch, F. Somma, C. Giampaolo, G. P. Pazzi, P. Fabeni and S. Zazubovich, Photoluminescence of Cs_4PbBr_6 crystals and thin films, *Chem. Phys. Lett.*, 1999, **306**, 280–284.

22 D. Q. Chen, Z. Y. Wan, X. Chen, Y. J. Yuan and J. S. Zhong, Large-scale room-temperature synthesis and optical properties of perovskite-related Cs_4PbBr_6 fluorophores, *J. Mater. Chem. C*, 2016, **4**, 10646–10653.

23 A. J. Zarur and J. Y. Ying, Reverse microemulsion synthesis of nanostructured complex oxides for catalytic combustion, *Nature*, 2000, **403**, 65–67.

24 R. Saran and R. J. Curry, Lead sulphide nanocrystal photodetector technologies, *Nat. Photonics*, 2016, **10**, 81–92.

25 P. H. Rekemeyer, C. H. M. Chuang, M. G. Bawendi and S. Gradecak, Minority Carrier Transport in Lead Sulfide Quantum Dot Photovoltaics, *Nano Lett.*, 2017, **17**, 6221–6227.

26 A. Sadhu, Y. Y. Guo, T. Salim, Q. D. Sun, S. G. Mhaisalkar, T. C. Sum and L. H. Wong, Elucidating the Role of Chalcogenide-Based Interface Passivators in Enhancing the Stability of Perovskite Solar Cells, *Adv. Funct. Mater.*, 2023, **33**, 12.

27 Y. M. Chen, Y. Zhou, Q. Zhao, J. Y. Zhang, J. P. Ma, T. T. Xuan, S. Q. Guo, Z. J. Yong, J. Wang, Y. Kuroiwa, C. Moriyoshi and H. T. Sun, $Cs_4PbBr_6/CsPbBr_3$ Perovskite Composites with Near-Unity Luminescence Quantum Yield: Large-Scale Synthesis, Luminescence and Formation Mechanism, and White Light-Emitting Diode Application, *ACS Appl. Mater. Interfaces*, 2018, **10**, 15905–15912.

28 L. L. Wang, H. Liu, Y. H. Zhang and O. F. Mohammed, Photoluminescence Origin of Zero-Dimensional Cs_4PbBr_6 Perovskite, *ACS Energy Lett.*, 2020, **5**, 87.

29 F. Krieg, S. T. Ochsenbein, S. Yakunin, S. ten Brinck, P. Aellen, A. Suess, B. Clerc, D. Guggisberg, O. Nazarenko, Y. Shynkarenko, S. Kumar, C. J. Shih, I. Infante and M. V. Kovalenko, Colloidal $CsPbX_3$ (X = CI, Br, I) Nanocrystals 2.0: Zwitterionic Capping Ligands for Improved Durability and Stability, *ACS Energy Lett.*, 2018, **3**, 641–646.

30 J. Z. Song, J. H. Li, X. M. Li, L. M. Xu, Y. H. Dong and H. B. Zeng, Quantum Dot Light-Emitting Diodes Based on Inorganic Perovskite Cesium Lead Halides ($CsPbX_3$), *Adv. Mater.*, 2015, **27**, 7162–+.

31 G. Q. Tong, H. Li, Z. F. Zhu, Y. Zhang, L. W. Yu, J. Xu and Y. Jiang, Enhancing Hybrid Perovskite Detectability in the Deep Ultraviolet Region with Down-Conversion Dual-Phase ($CsPbBr_3$-Cs_4PbBr_6) Films, *J. Phys. Chem. Lett.*, 2018, **9**, 1592–1599.

32 K. Y. Wang, Y. Yuan, S. J. Du, Q. Yao, J. Zhang, C. Y. Shang, C. Q. Li, H. Q. Sun, W. W. Zhang, J. X. Ding and T. L. Zhou, Understanding of the Photoluminescence Mechanism Based on Zero-Dimensional Cs4PbBr$_{6-m}$X$_m$ (X = Cl, I) Single Crystals, *J. Phys. Chem. C*, 2021, **125**, 15223–15232.

33 G. Kresse and J. Furthmuller, Efficiency of ab-initio total energy calculations for metals and semiconductors using a plane-wave basis set, *Comput. Mater. Sci.*, 1996, **6**, 15–50.

34 G. Kresse and D. Joubert, From ultrasoft pseudopotentials to the projector augmented-wave method, *Phys. Rev. B*, 1999, **59**, 1758–1775.

35 V. Wang, N. Xu, J. C. Liu, G. Tang and W. T. Geng, VASPKIT: A user-friendly interface facilitating high-throughput computing and analysis using VASP code, *Comput. Phys. Commun.*, 2021, **267**, 19.

36 J. Almutlaq, J. Yin, O. F. Mohammed and O. M. Bakr, The Benefit and Challenges of Zero-Dimensional Perovskites, *J. Phys. Chem. Lett.*, 2018, **9**, 4131–4138.

37 Q. A. Akkerman, S. Park, E. Radicchi, F. Nunzi, E. Mosconi, F. De Angelis, R. Brescia, P. Rastogi, M. Prato and L. Manna, Nearly Monodisperse Insulator Cs_4PbX_6 (X = Cl, Br, I) Nanocrystals, Their Mixed Halide Compositions, and Their Transformation into $CsPbX_3$ Nanocrystals, *Nano Lett.*, 2017, **17**, 1924–1930.

38 X. D. Wu, R. J. Xu, X. L. Li, R. S. Zeng and B. B. Luo, Amino Acid-Assisted Preparation of Homogeneous PbS/$CsPbBr_3$ Nanocomposites for Enhanced Photoelectrocatalytic CO_2 Reduction, *J. Phys. Chem. C*, 2022, **126**, 15744–15751.

39 L. Yang, D. M. Li, C. Wang, W. Yao, H. Wang and K. X. Huang, Room-temperature synthesis of pure perovskite-related Cs_4PbBr_6 nanocrystals and their ligand-mediated evolution into highly luminescent $CsPbBr_3$ nanosheets, *J. Nanopart. Res.*, 2017, **19**, 13.

40 D. Han, H. L. Shi, W. M. Ming, C. K. Zhou, B. W. Ma, B. Saparov, Y. Z. Ma, S. Y. Chen and M. H. Du, Unraveling luminescence mechanisms in zero-dimensional halide perovskites, *J. Mater. Chem. C*, 2018, **6**, 6398–6405.

41 Y. K. Jung, K. T. Butler and A. Walsh, Halide Perovskite Heteroepitaxy: Bond Formation and Carrier Confinement at the PbS-$CsPbBr_3$ Interface, *J. Phys. Chem. C*, 2017, **121**, 27351–27356.